# Analysis of PWM Voltage Detection Delay for Current Source Type Electric Motor Emulator

Gensui Tanaka
*Dept. of Technology of Science Innovation*
*Nagaoka University of Technology*
Nagaoka, Japan
s203164+tanaka@stn.nagaokaut.ac.jp

Hiroki Watanabe
*dept. of Electrical, Electronics, and Information Engineering*
*Nagaoka University of Technology*
Nagaoka, Japan
hwatanabe@vos.nagaokaut.ac.jp

Jun-ichi Itoh
*dept. of Technology of Science Innovation*
*Nagaoka University of Technology*
Nagaoka, Japan
itoh@vos.nagaokaut.ac.jp

***Abstract*— This paper focuses on input voltage detection for an electric motor emulator (EME), which imitates various motor operations accurately. The EME has to detect the PWM voltage of an inverter under test (IUT) as the input voltage of the EME. The delay in the PWM voltage detection reduces the emulation accuracy. This paper reveals the relationship between the cutoff frequency of a low-pass filter (LPF) for voltage detection and the current control bandwidth of both the IUT and the EME. The analysis result mentions that a low cutoff frequency, such as 1 kHz, is acceptable under the current control bandwidth of 100 Hz in the IUT. In addition, the cutoff frequency of the LPF should be set to a frequency larger than eight times the current control bandwidth of the IUT to keep the transient response in any conditions. Furthermore, it is verified that the phase lead compensation keeps the current response when the cutoff frequency and the current control bandwidth of the IUT are close.**

***Keywords—electric motor emulator, power hardware-in-the-loop (PHIL), current control, low-pass filter (LPF)***

## I. INTRODUCTION

Recently, electrical motor emulator (EME) systems, which imitate various motor behaviors by a power converter, are attracted to the development of adjustable speed drive systems, such as EVs [1-3]. The EME has significant advantages, such as the easy test of an inverter without a large motor bench, changing the motor parameters, and testing conditions, including rotational speed and load torque. Therefore, the EME reduces the cost and time to develop a motor drive system, which contributes to the further spread of EVs.

The accuracy of the EME is affected by the detection of the output voltage of the inverter under test (IUT), which is the same as the input voltage of the EME [4-7]. One of the difficulties of the EME is that the EME has to detect the voltage from the PWM waveform of the IUT output voltage, which is a pulsed voltage generated by the PWM. Thus, accurate and fast voltage detection methods are required for the EME. In [4], the voltage command of the IUT is sent to the controller of the EME instead of the voltage detection. This method will reduce hardware and computational costs and improve emulation accuracy. However, the output of the IUT controller is needed to use the output voltage command of the IUT. Ref. [5] uses a comparator-based circuit to directly sample the PWM voltage at the logic level. This method has a very low delay due to the use of 200 MHz sampling by an FPGA. However, this method requires a high-performance controller in the EME.

The transient response and stability of the EME depend on voltage detection delay. Thus, the EME uses fast voltage detection methods [8-9]. A low-pass filter (LPF) is a simple method for detecting the modulated voltage from the PWM voltage. However, detection delay is an issue for the EME because it reduces stability and limits the gain in the feedback system. In contrast, the controller with a voltage detection method that is too fast causes expenses. The detection speed has one of the tread-off relations between performance and cost. However, past literature has not clarified the relationship between voltage detection delay and EME performance. The cost of implementation is reduced by using LPF to detect the output voltage of the IUT while maintaining the current response of the EME.

This paper analyzes the effect of the voltage detection delay on the performance of the EME. The new contribution of this paper is that the requirement for voltage detection in the current source type EME is revealed in terms of stability and keeping the current response of the EME. As a result, the cost of the EME will decrease because the too-fast voltage detection is not needed. The relationship between the cutoff frequency of the LPF for PWM voltage detection and the current control bandwidth of the IUT is analyzed using Bode diagrams and pole plots. The limit of the cutoff frequency is revealed in order to keep the accuracy of the current response of the IUT. In addition, the desired current response is achieved by applying the phase lead compensation when the voltage detection with the LPF does not keep the accuracy of the current response of the IUT.

This paper is organized as follows: First, the EME configuration is introduced. Second, the acceptable cutoff frequency is derived from the relationship between the LPF and the current control bandwidth. Third, the phase lead compensation improves the transient response. Finally, the simulation and experimental results demonstrate the validity of the analysis results.

## II. CURRENT SOURCE TYPE MOTOR EMULATOR

Fig. 1 shows an inverter test system configuration using a current source type EME. The EME is connected to the IUT with only three-phase power lines and position or speed sensor lines, as well as an actual motor. This paper selects an inductor and a three-phase inverter as the coupling and power converter for the EME. This configuration is the same as that of a PWM rectifier. Thus, the controller of the EME has the same configuration as the controller for the three-phase PWM rectifiers. The detected output phase voltage of the IUT is sent to the motor model implemented in the EME controller. The motor current command of the EME is calculated by a motor

model simultaneously with the motor speed and torque. The EME imitates the motor behavior by controlling the motor current due to the current control.

The state equation of an interior permanent magnet synchronous motor (IPMSM) is implemented as the motor model of the motor under test (MUT). The state equation of an IPMSM based on the dq-axis is expressed as

$$P\begin{bmatrix} i_d \\ i_q \end{bmatrix} = \begin{bmatrix} -\frac{R_a}{L_d} & \omega_{re}\frac{L_q}{L_d} \\ -\omega_{re}\frac{L_q}{L_d} & -\frac{R_a}{L_q} \end{bmatrix}\begin{bmatrix} i_d \\ i_q \end{bmatrix} + \begin{bmatrix} \frac{v_d}{L_d} \\ \frac{v_q}{L_q} \end{bmatrix} + \begin{bmatrix} 0 \\ -\frac{\omega_{re}\psi_m}{L_q} \end{bmatrix} \quad \cdots\cdots(1),$$

where $i_d$ and $i_q$ are the dq-axis current, $v_d$ and $v_q$ are the dq-axis voltage, $R_a$ is the armature resistance, $L_d$ and $L_q$ are the dq-axis synchronous inductance, $\omega_{re}$ is the electric angler frequency, $\psi_m$ is the flux linkage of the permanent magnet, and $P$ is the differential operator.

Here, the output torque $T_{out}$ and the relationship between the electric angular frequency and output torque on the dq-axis are expressed as

$$T_{out} = p\{\psi_m i_q + (L_d - L_q) i_d i_q\} \quad \cdots\cdots(2),$$

$$P\omega_{re} = \frac{p}{J}(T_{out} - T_L) \quad \cdots\cdots(3),$$

where $T_L$ is the load torque, $p$ is the pares of poles, and $J$ is the inertia of the motor.

The current commands are obtained by solving the differential equations (1), (2), and (3) using the backward Euler method in a DSP.

Table 1 shows the circuit parameter, and Table 2 shows the MUT parameter. The EME circuit requires a power rating and DC link voltage higher than one of the IUT. The calculation period and the deletion of the switching devices determine the switching frequency of the EME.

## III. Clarification of Acceptable Voltage Detection Delay Time

### A. Analysis by Bode diagram

This section analyzes the relationship between the cutoff frequency of the LPF and the current control bandwidth of both the IUT and the EME based on the Bode diagram. Note that the parameters in Table 1 and Table 2 are used in the analysis.

Fig. 2 shows the analysis model based on the dq-axis. In this paper, the field-oriented control is implemented in the IUT controller. The q-axis current command is determined from the torque command, and the d-axis current command is set to zero. Thus, the IUT controller has no speed control, and a constant speed is assumed. In this paper, the motor speed is set to 3600 r/min. This configuration is the same as the speed controlled by the load machine connected to the IUT in the inverter test system, which uses a motor bench. In addition, the IUT controller utilizes the decoupling control for an IPMSM in order to cancel the cross-coupling terms between the dq-axis. The input voltages of the motor model

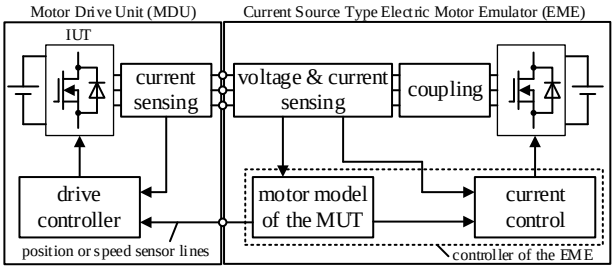


Fig. 1 Configuration of an inverter test system using an EME.

Table 1 Parameter of the circuit.

| Parameter | Symbol | Value |
|---|---|---|
| DC link voltage of IUT | $V_{dc\_IUT}$ | 280 V |
| DC link voltage of ME | $V_{dc\_ME}$ | 320 V |
| Coupling inductor | $L_{coup}$ | 1.73mH |
| Switching frequency of IUT | $f_{sw\_IUT}$ | 10 kHz |
| Switching frequency of ME | $f_{sw\_ME}$ | 40 kHz |

Table 2 Parameter of an IPMSM.

| Parameter | Symbol | Value |
|---|---|---|
| Output power | $P_n$ | 3.7 kW |
| Maximum speed | $\omega_n$ | 7200 r/min |
| Output torque | $T_n$ | 4.91 N·m |
| Pole pairs | $p$ | 2 |
| Winding resistance | $R$ | 116 mΩ |
| d-axis inductance | $L_d$ | 2.59 mH |
| q-axis inductance | $L_q$ | 3.63 mH |
| flux linkage of permanent magnet | $\Psi_m$ | 0.0905 Wb |
| Moment of inertia | $J$ | $30\times10^{-4}$ N·m |

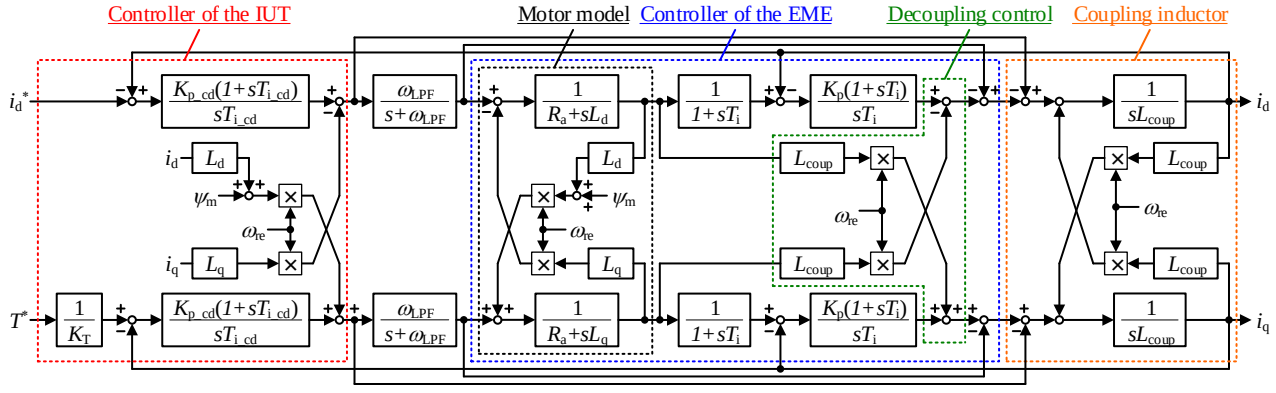


Fig. 2 Analysis model for the relationship between the cutoff frequency of the LPF and the responses of the current control for the IUT.

are the output voltages of the IUT detected by the LPF. Thus, the LPFs are inserted in front of the motor model in Fig. 2.

Fig. 3 shows the simplified model shown in Fig. 2. It is assumed that the interference between the dq-axis of the IPMSM and the coupling inductor are eliminated through decoupling control for simplification of the model. The gain of the IUT current control is designed to obtain a first-order delay response with the integration time as the electrical time constant of the motor. The gain of the EME current control is decided by comparison with the secondary standard form, with the coupling inductor serving as the control target. Consequently, the open-loop transfer function is a series connection of the integral element of the IUT current control system, the LPF, and the second-order standard form.

Fig. 4 shows the open loop Bode diagram of the simplified model as shown in Fig. 3. As shown in Fig. 4(a), the gain decreases at -20 dB/dec at a frequency up to $f_{IUT}$ and by -40 dB/dec above $f_{IUT}$ when the cutoff frequency of the LPF is higher than the current control bandwidth of the IUT. As a result, the gain crossover angular frequency of the open loop transfer function is $f_{LPF}$, intersecting 0 dB at -20 dB/dec. In contrast, as shown in Fig. 4(b), the slope is steeper than -20 dB/dec and crosses 0 dB at a maximum of -40 dB/dec when the $f_{LPF}$ is close to or lower than the $f_{IUT}$. In the open loop Bode diagram, it is recommended that the cutoff frequency of the LPF be set at a higher than the current control bandwidth of the IUT in order to achieve a slower gain gradient near the gain crossover angular frequency.

Fig. 5 shows the closed loop Bode diagram for cutoff frequency variation. The IUT current control bandwidth is set to 500 Hz, and the EME current control bandwidth is set to 2000 Hz, respectively. A gain peak occurs when the LPF cutoff frequency is 3 kHz or lower, which may worsen the current response. In contrast, a gain peak dose does not appear, and there is little effect on the current response when the LPF cutoff frequency is 4 kHz or higher. Consequently, the voltage detection delay should be acceptable when the LPF cutoff frequency is set to eight times or more than the IUT current control bandwidth.

Fig. 6 shows the closed-loop Bode diagram for IUT current control bandwidth variation. Note that the cutoff frequency of the LPF is 1 kHz, and the EME current control bandwidth is 2000 Hz. Decreasing the IUT current control

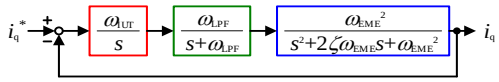


Fig. 3 Simplified model.

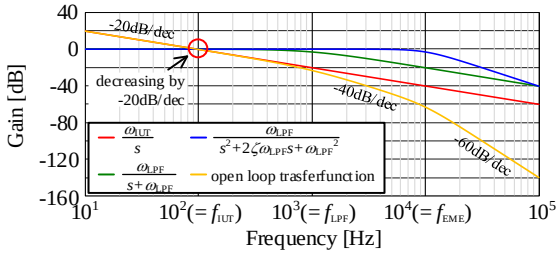


(a) $f_{IUT}$ = 100 Hz, $f_{LPF}$ = 1000 Hz, $f_{EME}$ = 10000 Hz.

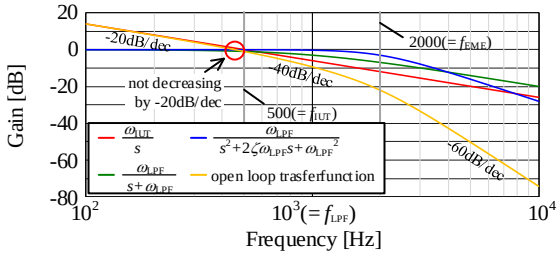


(b) $f_{IUT}$ = 500 Hz, $f_{LPF}$ = 1000 Hz, $f_{EME}$ = 2000 Hz.

Fig. 4 Open-loop Bode diagram of the model shown in Fig. 3.

bandwidth suppresses the gain peak. In particular, the gain peak does not occur when the IUT current control bandwidth is 100 Hz. This is because the cutoff frequency of the LPF and the IUT current control bandwidth are sufficiently disparate, as explained in Fig. 4. Therefore, applying an LPF with a low cutoff frequency is acceptable while keeping the current response when the current control bandwidth of the IUT is low.

Fig. 7 shows the closed-loop Bode diagram for EME current control bandwidth variation. Note that the IUT current control bandwidth is 500 Hz, and the cutoff frequency of the LPF is 1 kHz. Increasing the EME current control bandwidth suppressed the gain peak. However, the reduction in effect is less significant than when the IUT current control bandwidth is lowered. This is because the gain crossing angular frequency remains unaffected mainly when the EME current control bandwidth is designed to be sufficiently high relative to the EME current control bandwidth, as shown in Fig. 4(b).

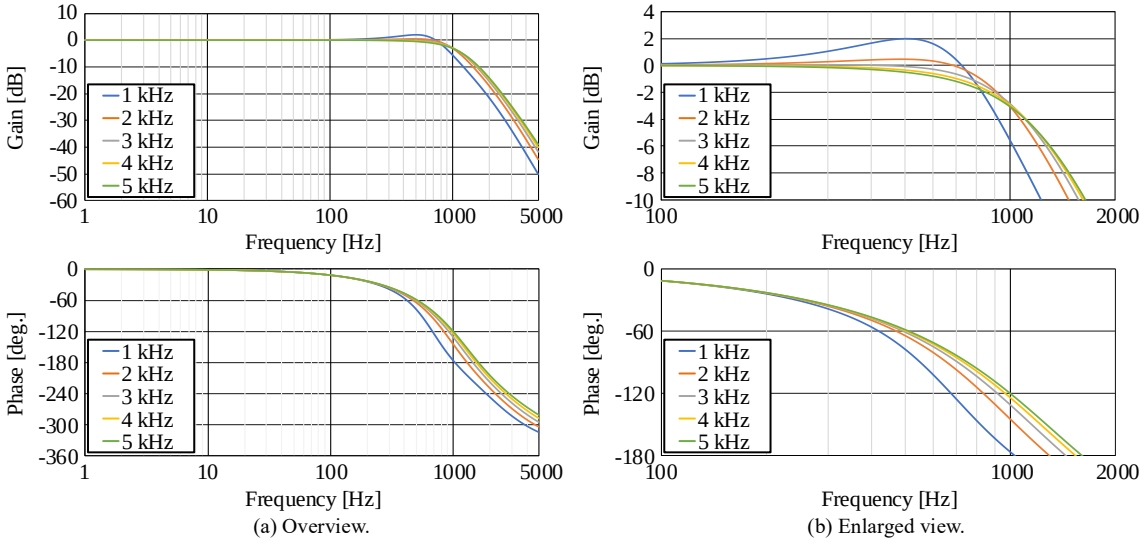


(a) Overview. (b) Enlarged view.

Fig. 5 Closed-loop Bode diagram for cutoff frequency variation.

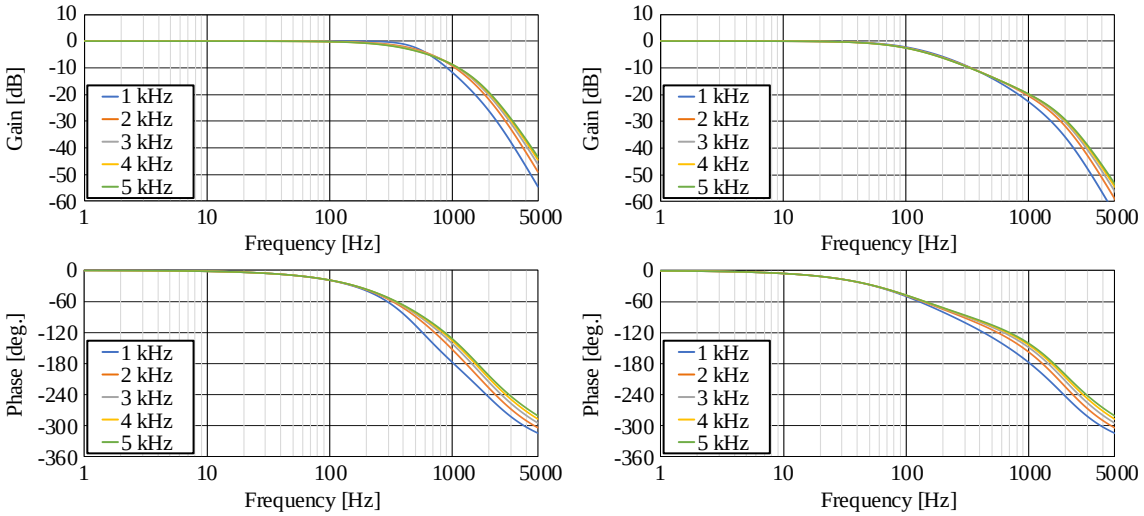


(a) 300 Hz. (b) 100 Hz.

Fig. 6 Closed-loop Bode diagram for IUT current control bandwidth variation.

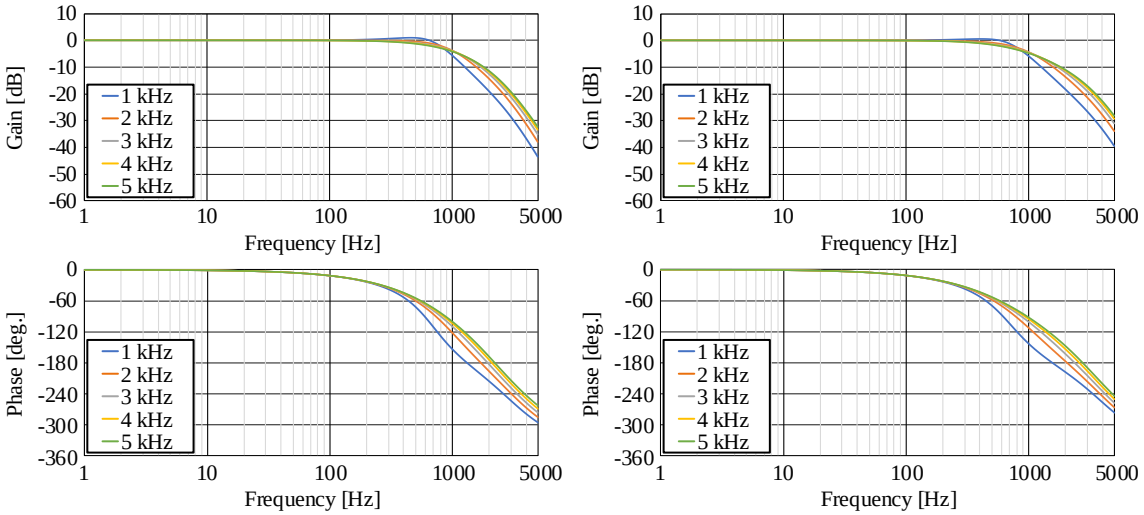


(a) 3000 Hz. (b) 4000 Hz.

Fig. 7 Closed-loop Bode diagram for EME current control bandwidth variation.

### B. *Analysis by pole plot*

This section analyzes the cause of the gain peak on the Bode diagram when using an LPF with a low cutoff frequency, such as 1 kHz, based on the root locus. The gain peak is suppressed by decreasing the current control bandwidth of the IUT.

Fig. 8 shows the pole plot for cutoff frequency variation. The dominant pole is the real pole when the LPF is not used. In contrast, the dominant poles are complex conjugate poles when the LPF is used. The poles are close to the pole when the LPF is not used, according to an increase in the cutoff frequency of the LPF. This result is the same as in Fig. 5. The poles caused by inserting the LPF are the real poles when the cutoff frequency is set to 4 kHz or 5 kHz. In contrast, these poles are the complex conjugate poles when the cutoff frequency of the LPF is set to 3 kHz or less. As a result, an overshoot occurs in the closed-loop Bode diagram, as shown in Fig. 5.

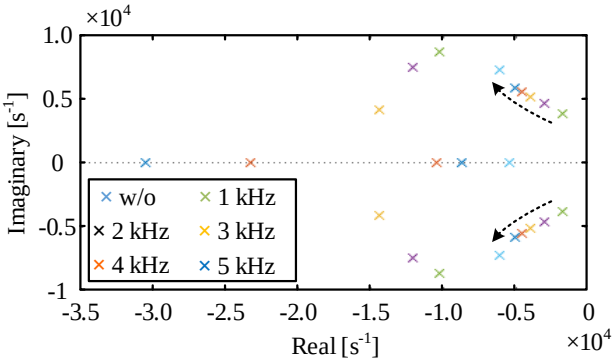


Fig. 8 Pole plot for cutoff frequency of LPF variation.

## IV. Improvement of Transient Response with Phase Lead Compensation

Chapter III clarified the acceptable voltage detection delay. However, the cutoff frequency of the LPF also has to be high in order to accept the voltage detection delay when the current control bandwidth of the IUT is high. In this case, there is concern that the voltage detection accuracy will deteriorate due to the remaining harmonic components, making it impossible to calculate the motor current accurately. In contrast, the motor current is calculated accurately when the cutoff frequency of the LPF is low enough relative to the switching frequency of the IUT. Although, the voltage detection delay is not accepted, and the current response

deteriorates. Therefore, the current response is able to be improved by implementing phase lead compensation when using an LPF with a low cutoff frequency.

Fig. 9 shows the Bode diagram of phase lead compensation. The transfer function with the frequency characteristic shown in Fig. 6 is expressed as

$$K(s) = K\frac{T_{comp}s+1}{\alpha T_{comp}s+1} \quad \text{.....(4)},$$

where $K$ is the compensation gain coefficient, $T_{comp}$ is the reciprocal of the break angler frequency $\omega_{comp}$, and $\alpha$ is the coefficient that determines the gain compensation range.

The detected voltage using the LPF is compensated by inserting (4) before the motor model in the EME controller. A linear approximation of the gain characteristics of the LPF shows that the gain is 0 dB up to the cutoff frequency, and then it decays at -20 dB/dec. Therefore, in order to cancel the gain characteristics of the LPF, $K$ should be set to 1, $T_{comp}$ should be set to $1/(2\pi f_{LPF})$, and $\alpha$ should be set to the frequency range to be compensated.

Fig. 10 shows the closed loop Bode diagram with the phase lead compensation. Note that $K$ is set to 1, $T_{comp}$ is set to $1/(2\pi f_{LPF})$, and $\alpha$ is set to 0.01. Gain peak and phase delays occur in cases without compensation. In contrast, the same characteristics as those without LPF insertion are obtained by applying compensation. Therefore, the desired current response is maintained even when using an LPF with a low cutoff frequency. This is achieved by compensating for the unacceptable voltage detection delay with phase lead compensation.

Fig. 11 shows the pole plot when applying the phase lead compensation. The dominant pole is the complex conjugate pole without the phase lead compensation. In contrast, the dominant pole becomes the real pole when the phase lead compensation is applied. In addition, the poles with phase lead compensation are located in the same place as those without the LPF, as shown in Fig. 8. Therefore, applying the phase lead compensation removes the influence of utilizing the LPF. These results agree with the analysis using the Bode diagram shown in Fig. 9.

## V. Experimental Result

Fig. 12 shows the difference in the current response with and without an LPF, with an acceptable detection delay. Note that the LPF is not utilized in Fig. 8(a) to verify its influence. Instead, the voltage command is directly inputted from the IUT controller to the EME controller, providing a clear view of the absence of the LPF. An overshoot is not observed in the q-axis current response when an LPF is not utilized. Similarly, an overshoot does not occur when the IUT output voltage is detected by an LPF with a cutoff frequency of 4 kHz. Consequently, the current response is equivalent when an LPF has an acceptable voltage detection delay time.

Fig. 13 shows the current response using an LPF with an unacceptable voltage detection delay. Note that the cutoff frequency of the LPF is 1 kHz. Each gain of the phase lead compensation is set to $K = 1$, $T_{comp} = 1/(2\pi f_{LPF})$, and $\alpha = 0.2$. It is possible to fully compensate the LPF on the transfer function by using a small $\alpha$ value, as shown in Fig. 7. However, the EME controller becomes unstable due to (4) being a pseudo-differential form. The determination of the optimal alpha value represents a topic for future research. As shown in Fig. 8(a), the utilization of an LPF with a 1 kHz cutoff frequency results in an overshoot of the q-axis current and distortion of the phase current.

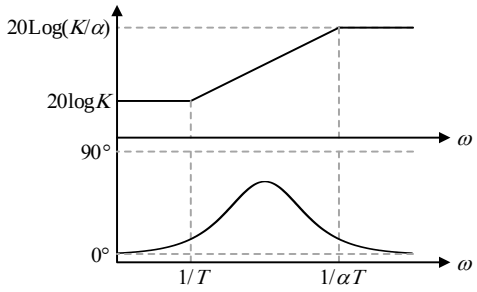

Fig. 9 Open loop Bode diagram of phase lead compensation.

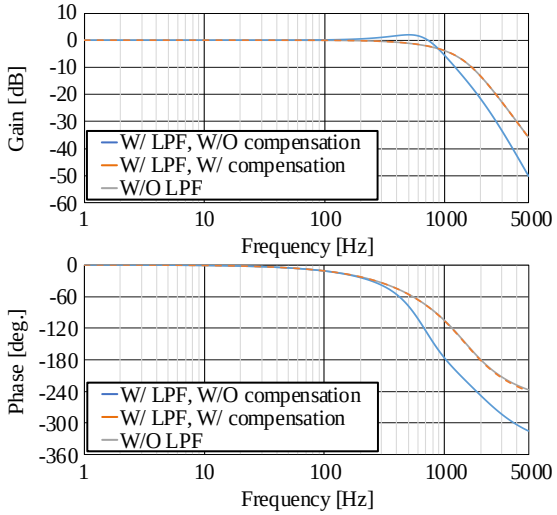

Fig. 10 Closed loop Bode diagram with phase lead compensation.

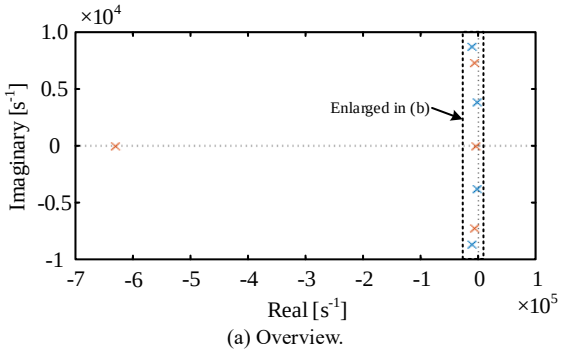

(a) Overview.

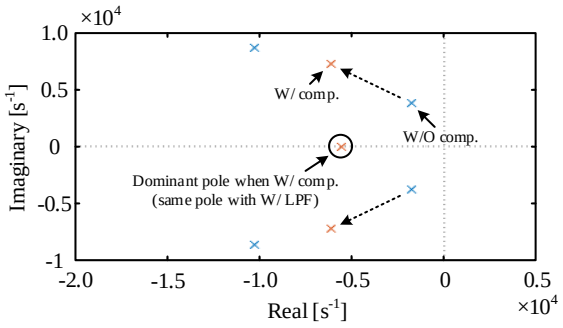

(b) Enlarged view.

Fig. 11 Pole plot when applying phase lead compensation.

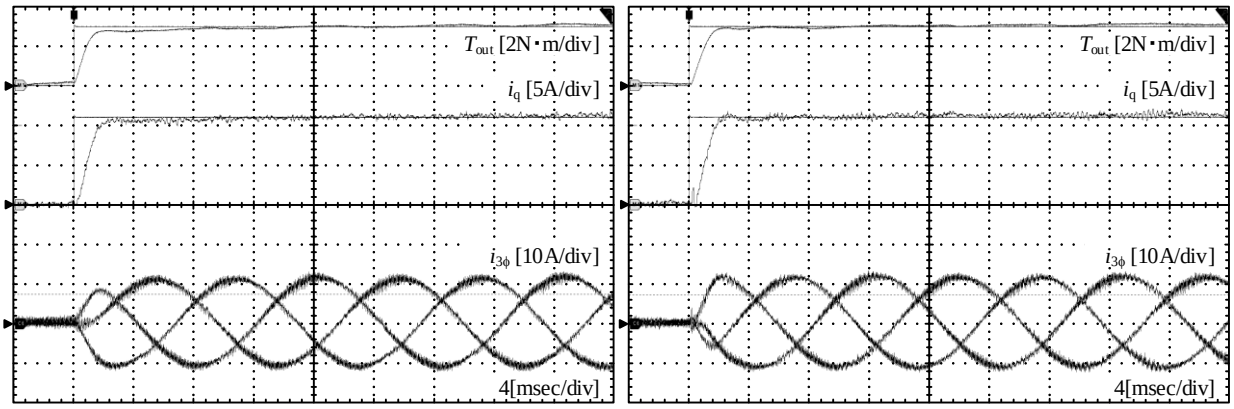


(a) W/O LPF. (b) W/ LPF ($f_{LPF}$ = 4 kHz).

Fig. 12 Step response with LPF having an acceptable detection delay.

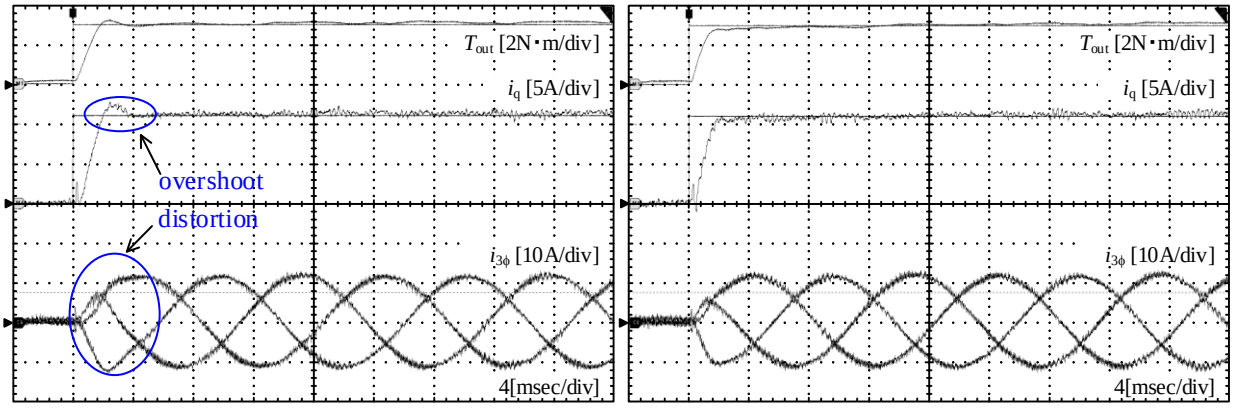


(a) W/O compensation. (b) W/ compensation.

Fig. 13 Step response with LPF having an unacceptable detection delay with phase lead compensation.

## VI. Conclusion

This paper clarified the delay time required to maintain the current response of the IUT. The LPF with a low cutoff frequency, such as 1/10 of the carrier frequency, causes the gain peak in the closed-loop Bode diagram of the current control of the IUT. In contrast, the LPF with a cutoff frequency of 4 kHz does not cause the gain peak in the closed-loop Bode diagram of the current control of the IUT. Thus, the desired current response is maintained by designing the LPF cutoff frequency to be more than eight times the IUT current control bandwidth. This indicates that not only is the current response maintained, but the LPF is also utilized for PWM voltage detection by selecting the cutoff frequency appropriately. On the other hand, the phase lead compensation is applied in order to achieve the desired current response when utilizing an LPF with an unacceptable voltage detection delay. Analysis and experimental results show that the desired current response can be achieved by applying for phase advance compensation when the desired delay time cannot be met using an LPF.

## References

[1] K. Etzold et al., "Function Development With an Electric-Machine-in-the-Loop Setup: A Case Study," in IEEE Transactions on Transportation Electrification, vol. 5, no. 4, pp. 1419-1429, Dec. 2019.

[2] A. S. Abdelrahman, K. S. Algarny and M. Z. Youssef, "A Novel Platform for Powertrain Modeling of Electric Cars With Experimental Validation Using Real-Time Hardware in the Loop (HIL): A Case Study of GM Second Generation Chevrolet Volt," in IEEE Transactions on Power Electronics, vol. 33, no. 11, pp. 9762-9771, Nov. 2018.

[3] Q. Li, D. Wang, J. Lin, F. Jian, Z. Wang and C. Ma, "Improving Dynamic Accuracy of the Electric Motor Emulator at High Speed via MIMO Design Method," in IEEE Transactions on Power Electronics, vol. 37, no. 12, pp. 14395-14407, Dec. 2022.

[4] Y. Qi, K. Ma, and W. Tang, "Full-Bandwidth Mission Profile Emulation of the Electric Machine System With Voltage Reference Signal Transmission," in IEEE Transactions on Power Electronics, vol. 37, no. 3, pp. 3473-3483, March 2022.

[5] Y. Luo, M. A. Awal, W. Yu, and I. Husain, "FPGA-Based High-Bandwidth Motor Emulator for Interior Permanent Magnet Machine Utilizing SiC Power Converter," in IEEE Journal of Emerging and Selected Topics in Power Electronics, vol. 9, no. 4, pp. 4340-4353, Aug. 2021.

[6] K. S. Amitkumar, P. Pillay and J. Bélanger, "An Investigation of Power-Hardware-in-the-Loop- Based Electric Machine Emulation for Driving Inverter Open-Circuit Faults," in IEEE Transactions on Transportation Electrification, vol. 7, no. 1, pp. 170-182, March 2021.

[7] Y. -R. Lee, Y. -C. Kwon and S. -K. Sul, "DC-Link Voltage Design of High-Bandwidth Motor Emulator for Interior Permanent-Magnet Synchronous Motors," 2018 IEEE Energy Conversion Congress and Exposition (ECCE), Portland, OR, USA, 2018, pp. 4453-4459.

[8] K. Ma, S. Xia, Y. Qi, X. Cai, Y. Song, and F. Blaabjerg, "Power-Electronics-Based Mission Profile Emulation and Test for Electric Machine Drive System—Concepts, Features, and Challenges," in IEEE Transactions on Power Electronics, vol. 37, no. 7, pp. 8526-8542, July 2022.

[9] Tung-Hai Chin, M. Nakano, and T. Hirayama, "Accurate measurement of instantaneous values of voltage, current and power for power electronics circuits," PESC 98 Record. 29th Annual IEEE Power Electronics Specialists Conference (Cat. No.98CH36196), Fukuoka, Japan, 1998, pp. 302-307 vol. 1